



Retrospective 4D MR image construction from free-breathing slice Acquisitions: A novel graph-based approach



Yubing Tong^a, Jayaram K. Udupa^{a,*}, Krzysztof C. Ciesielski^{a,b}, Caiyun Wu^a, Joseph M. McDonough^c, David A. Mong^c, Robert M. Campbell Jr.^c

^a Medical Image Processing Group, Department of Radiology, University of Pennsylvania, Philadelphia, PA, 19104 United States

^b Department of Mathematics, West Virginia University, Morgantown, WV, 26505 United States

^c Center for Thoracic Insufficiency Syndrome, Children's Hospital of Philadelphia, Philadelphia, PA, 19104 United States

ARTICLE INFO

Article history:

Received 2 January 2016

Revised 5 July 2016

Accepted 9 August 2016

Available online 13 August 2016

Keywords:

Dynamic MRI

4D image construction

Path optimization

Lung imaging

Thoracic insufficiency syndrome

ABSTRACT

Purpose: Dynamic or 4D imaging of the thorax has many applications. Both prospective and retrospective respiratory gating and tracking techniques have been developed for 4D imaging via CT and MRI. For pediatric imaging, due to radiation concerns, MRI becomes the de facto modality of choice. In thoracic insufficiency syndrome (TIS), patients often suffer from extreme malformations of the chest wall, diaphragm, and/or spine with inability of the thorax to support normal respiration or lung growth (Campbell et al., 2003, Campbell and Smith, 2007), as such patient cooperation needed by some of the gating and tracking techniques are difficult to realize without causing patient discomfort and interference with the breathing mechanism itself. Therefore (ventilator-supported) free-breathing MRI acquisition is currently the best choice for imaging these patients. This, however, raises a question of how to create a consistent 4D image from such acquisitions. This paper presents a novel graph-based technique for compiling the best 4D image volume representing the thorax over one respiratory cycle from slice images acquired during unencumbered natural tidal-breathing of pediatric TIS patients.

Methods: In our approach, for each coronal (or sagittal) slice position, images are acquired at a rate of about 200–300 ms/slice over several natural breathing cycles which yields over 2000 slices. A weighted graph is formed where each acquired slice constitutes a node and the weight of the arc between two nodes defines the degree of contiguity in space and time of the two slices. For each respiratory phase, an optimal 3D spatial image is constructed by finding the best path in the graph in the spatial direction. The set of all such 3D images for a given respiratory cycle constitutes a 4D image. Subsequently, the best 4D image among all such constructed images is found over all imaged respiratory cycles. Two types of evaluation studies are carried out to understand the behavior of this algorithm and in comparison to a method called Random Stacking – a 4D phantom study and 10 4D MRI acquisitions from TIS patients and normal subjects. The 4D phantom was constructed by 3D printing the pleural spaces of an adult thorax, which were segmented in a breath-held MRI acquisition.

Results: Qualitative visual inspection via cine display of the slices in space and time and in 3D rendered form showed smooth variation for all data sets constructed by the proposed method. Quantitative evaluation was carried out to measure spatial and temporal contiguity of the slices via segmented pleural spaces. The optimal method showed smooth variation of the pleural space as compared to Random Stacking whose behavior was erratic. The volumes of the pleural spaces at the respiratory phase corresponding to end inspiration and end expiration were compared to volumes obtained from breath-hold acquisitions at roughly the same phase. The mean difference was found to be roughly 3%.

* Corresponding author. Fax: 215 573 1811.

E-mail address: jay@mail.med.upenn.edu (J.K. Udupa).

Conclusions: The proposed method is purely image-based and post-hoc and does not need breath holding or external surrogates or instruments to record respiratory motion or tidal volume. This is important and practically warranted for pediatric patients. The constructed 4D images portray spatial and temporal smoothness that should be expected in a consistent 4D volume. We believe that the method can be routinely used for thoracic 4D imaging.

© 2016 Elsevier B.V. All rights reserved.

1. Introduction

1.1. Background

Dynamic 3D imaging, often referred to as 4D imaging, of various organ systems throughout the body is crucial to quantify organ displacements, visualize abdominal and thoracic organ motion, and assess mechanical functions of organs, which have found use in studying disease processes, their improved diagnosis, and planning of surgery, and radiation therapy (Tory et al., 2001; Nehmeh et al., 2004a). The focus of this paper is dynamic imaging of the thorax with emphasis on the lungs. Different modalities have been explored for 4D imaging of the lungs including time-resolved volumetric CT, MRI, PET, PET/CT and Ultra Sound imaging (Cai et al., 2011; Fayad and Lamare, 2013; Georg and Souvenir, 2008; Georg et al., 2008; Keall et al., 2004, 2007; Koste et al., 2006; Li et al., 2008; Liu et al., 2014; Low et al., 2003; Murphy et al., 2007; Nehmeh et al., 2004b; Remmert et al., 2007; Siebenthal et al., 2005, 2007; Tsoumpas et al. 2011; Wachinger et al., 2010, 2012; Wagshul et al. 2013; Wink et al. 2006; and Yang et al., 2008). Among these, CT, MRI, and Ultra Sound offer sufficient speed to acquire dynamic/motion information (Keall et al., 2007; Li et al., 2008; Low et al., 2003; and Wachinger et al., 2012). 4D-CT involves higher amount of radiation to the patient than static imaging due to increased scan time and does not provide sufficient information about displacements of soft-tissue objects because of low contrast among them (Keall et al., 2004, 2007; Koste et al., 2006; Wink et al., 2006; Li et al., 2009; Georg et al., 2008; and Yang et al., 2008). Ultra Sound causes shadowing effect from bone and has therefore limited utility in 4D imaging of the thorax (Wachinger et al. 2010, 2012). MRI offers excellent soft-tissue contrast and involves no radiation hazard, and hence, it is the modality of choice, especially for imaging the pediatric thorax (Nandalike, et al., 2013).

1.2. Rationale and related work

Because of the inherent speed limitations of MRI, three types of dynamic MRI approaches have evolved: the first based on fast 3D MRI sequences for real-time volumetric acquisitions (Wagshul et al., 2013), the second using fast 2D sequences for real-time slice acquisitions requiring some cooperation from the patient in the form of wearing a device or breath control (Li et al., 2009; Low et al., 2003; Nehmeh et al., 2004; Qi et al., 2013; Wink et al., 2006; Yang et al., 2008; and Zhang et al., 2008), and the third also using fast 2D sequences but with no such requirement that encumbers patient's free breathing (Liu et al., 2014; Siebenthal et al. 2005, 2007; and Wachinger et al. 2012). The approaches in the first group often sacrifice spatial and/or contrast resolution to achieve the necessary temporal resolution. The 2D sequences of the second and third group generally achieve better image quality than the first. However, if the first group can achieve adequate image quality for subsequent image analysis, it will be the ideal choice.

Approaches in the second group require some form of respiratory surrogate to acquire or estimate breathing signal and then use

it to monitor patient motion during image acquisition. Tidal volume has been widely used as the respiratory signal to show the phase location in one breathing period or as retrospective gating signal for CT/MRI scanning since tidal volume changes periodically with breathing (Yang et al., 2008; Zhang et al., 2008). Other measurements of respiratory signals include using a strain gauge inserted inside an adjustable belt (Wink et al., 2006), or by tracking external markers placed on patient's body such as in the abdomen (Nehmeh et al., 2004). Position signals recorded by a real time position management system (RPM) has also been adopted as ground truth of breathing signal for 4D reconstruction and image evaluation (Li et al., 2009; Low et al., 2003). However, respiratory signals measured from different external surrogates may not always be accurate and implementable. Remmert demonstrates a retrospective 4D-MRI technique (Remmert et al., 2007) on a dynamic phantom using an external signal for motion monitoring. The external signal was derived from the positional changes of the piston rod of the water pump, which may not be appropriate for use with human subjects. The pediatric subjects we deal with in our imaging application area often suffer from extreme malformations of their chest wall, diaphragm, and/or spine. As such the second group of methods is difficult to realize practically because of severe thoracic deformity (Campbell et al., 2003; Campbell and Smith, 2007). Moreover, we are interested in the mechanical function of the patient thorax in its natural malformed form in tidal breathing. Therefore, the third approach of free-breathing MRI acquisitions seems to be currently the ideal modality of imaging for these patients.

The premise of the third group of approaches is to construct the 4D image post-hoc by collecting together slices based on features extracted from the slice images (Cai et al., 2011; Liu et al., 2014; Wachinger et al., 2010, 2012; and Siebenthal et al., 2005, 2007). Manifold learning techniques have been employed to extract phase index as the respiratory signal in previous research (Georg and Souvenir, 2008; Georg et al. 2008; and Wachinger et al., 2010, 2012). Laplacian eigen maps (Georg and Souvenir, 2008; Georg et al. 2008) and isometric feature mapping, or Isomap (Wachinger et al., 2010, 2012), are used to determine the low-dimensional manifold embedded in high-dimensional image space. Each slice image frame is assigned a coordinate in low-dimensional space via Laplacian eigenmap transformation which is then used as the phase index in the respiratory period. After manifold learning is performed, registration is used to align all the local features/coordinates to achieve a globally consistent breathing signal. Manifold learning methods commonly make assumptions about the regularity of the respiratory motion and parameterize this motion with a one-dimensional amplitude or phase. Although respiration clearly shows a repetitive character, the reduction of respiratory organ deformation to one parameter neglects residual variability or pseudo-periodicity that is common. This may also lead to artifacts in the constructed images. Other features such as dynamic change of body area in the axial MR images is used as an internal respiratory surrogate to represent the breathing signal since normally body area would change periodically with the breathing motion (Cai et al., 2011; and Liu et al., 2014). This method seems to work only on axial images, and again for our very sick pediatric

patients, it may fail since the changes of their body region area are often very small.

These challenges led us to the development of a new approach for 4D MR image construction from free-breathing acquisitions that is suited for our application. In our set up, while the patient is under free breathing condition often under general anesthesia and ventilator support, slice images are acquired for each (coronal or sagittal) spatial slice location over several respiratory cycles. The basic idea of the 4D construction approach is to first find, for each respiratory phase for which data are gathered, the best 3D spatial volume image that can be compiled from the acquired slices. A graph-based path optimization algorithm is utilized for this purpose. Subsequently, these 3D images are concatenated over each respiratory cycle to form a 4D image. Finally, among all such 4D images, the best 4D image constituting one respiratory cycle is selected by systematically examining all constructed 4D images. These steps are described in Section 2. The method is evaluated by considering the smoothness/contiguity of the slices in the spatial and temporal dimensions, as described in Section 3. A phantom experiment is also described in Section 3 for evaluating the approach which involves 3D printed lung phantom derived from patient anatomy, immersing the phantom in a water bath, acquiring dynamic MR images, and evaluating the 4D construction against known ground truth. The paper concludes with some remarks in Section 4. We believe that the proposed approach has the following unique characteristics. (a) It is purely image based without the need for external devices to measure tidal volume or respiratory signal for the purpose of sorting images. (b) There is no need for any form of control of breathing. (c) There is no registration operation and computation is rapid. Some very preliminary results along the lines of the study in this paper were presented in the proceedings of the SPIE Medical Imaging 2014 conference (Tong et al., 2014).

2. 4D image construction method

2.1. Data acquisition

In our dynamic MR imaging set up, for each coronal (or sagittal) slice position in the thorax, slice images are acquired continuously at a rate of about 200 ms/slice over several tidal breathing cycles while the patient is under general anesthesia and ventilator support (for MRI acquisition details, see Section 3). This process produces typically several thousands of slices which contain both the anatomic spatial and dynamic information about the thorax. It is essential to form one consistent and well-defined 4D volume from these data in order to perform any meaningful image processing and analysis operation on these data to harness the dynamic information they embody.

2.2. Problem formulation

An ideal 4D image B of a body region (such as the thorax) of a patient is considered to be a time sequence $B(t)$, where a time marker t varies over a time interval $[0, \tau]$. For a fixed time instance $t \in [0, \tau]$, image $B(t)$ is interpreted as a 3D image, that is, as an intensity function defined on a fixed rectangular domain $\Omega = X \times Y \times Z \text{ mm}^3$. We assume that Ω is defined and fixed with respect to an imaging device xyz coordinate system, called the *scanner coordinate system*, SCS, in which the units are expressed in millimeters and the time-varying body region B is situated within this domain Ω . The data set provided by the imaging device is treated as a sampling of this idealized 4D image over space and time over several breathing cycles. Our goal is to use this sampled data set to arrive at an approximation of $B(t)$ for t varying over one full breathing cycle.

The data produced by our dynamic MR imaging system is in the form of a sequence $A = \{f_1, \dots, f_M\}$ of 2D images, each 2D image f_i being a slice of B for a fixed value $z \in Z$ and a time instance $t_i \in [0, \tau]$. Note here that A denotes the set of all slices that have been acquired over an entire patient scan session that extends over a time interval $[0, \tau]$. That is, f_i is a 2D image defined on $X \times Y$ for z and $f_i(x, y)$ is the intensity of B at (x, y, z) at the time instance t_i of acquisition. Each slice image f_i is acquired within a very short time interval such that the motion may be thought of as being frozen during that time. For each fixed z -position in SCS, slice acquisitions are made in this manner over several full breathing cycles and the process is moved to the next z -position, etc. The number of z -locations where the acquisition takes place, as well as the actual z -coordinates of these locations are known in this scheme. In what follows, we will denote them as z_1, \dots, z_K and treat Z as equal to $\{z_1, \dots, z_K\}$.

The acquisition scheme is graphically depicted in Fig. 1, where the line at the top of the figure indicates continuous timeline from start to end of a patient scan, and each time interval demarcated by a successive pair of vertical line segments indicates the time duration over which slice acquisitions (denoted by dots) are made for each z -location z_i . The lower portion of Fig. 1 is a graphical representation that will be used in our method. In this representation, the time interval corresponding to each z -location z_i is expanded and drawn as a horizontal dotted line. Each bold dot on this line represents an acquired slice image.

We think of the actual motion of $B(t)$ in tidal breathing as being quasi-periodic in the following sense. Consider the thorax and the breathing motion for example. Although it is a repetitive process, it cannot be considered to be mathematically strictly periodic. The subject may take a shallow versus a deeper breath, although we will rule out more severe disturbances such as deep inhalation/exhalation, swallowing, and coughing. The data are acquired for each z -location over a period of time to provide enough slices to describe the motion. This time period extends to several (4–8) breathing cycles. Mathematically, quasi-periodicity can be represented as a mapping φ from $[0, \tau]$ into a circle C , representing respiratory phase, with the property that for any time instances t and t' in $[0, \tau]$, if $\varphi(t) = \varphi(t')$ (i.e., the time instances point to the same phase of the breathing cycle), then the 3D images $B(t)$ and $B(t')$ are (approximately) equal. This is the key, since the acquisition schema does not provide us full 3D image $B(t)$ for any time instance t . So, during the construction process, some sections of the constructed $B(t)$ will actually be the sections of $B(t')$ for another time instance t' of the same (or similar) breathing phase (i.e., $\varphi(t') \approx \varphi(t)$). More specifically, our output – a digital approximation of one full breathing cycle – will be of the form of a mapping F from $Z \times T$ into 2D images on $X \times Y$, where T is a finite subset (digital approximation) of the phase circle C , and, for every $(z, t) \in Z \times T$, $F_{z, t}$ is one of the data images f_i for which $z_i = z$ and $\varphi(t_i) \approx t$, so that the resulting map F leads to the best 4D image representing a breathing cycle. Stating precisely, our problem is: *given the set of all slices A under the assumption of quasi-periodicity, find F .*

We construct our solution, map F , in three stages. In *Stage 1*, we associate with each slice f_i an approximate breathing phase $\varphi(t_i) \in C$ at which the slice was taken. We also determine a digital approximation T of C that will be used to express F . In *Stage 2*, for each breathing phase $t \in T$ and each slice f_i with $\varphi(t_i) = t$, we find a 3D scene F_t – a mapping from Z with $F_t(z) = F_{z, t} = f_i$, $z_j = z$ and $\varphi(t_i) \approx t$ – containing the slice f_i and optimal with respect to the criteria described below. These spatial 3D scenes will be combined together to yield several 4D scenes each representing a full breathing cycle. In *Stage 3*, we decide which of these 4D scenes is to be taken as output. The steps associated with these three stages are described below in the remainder of this section.

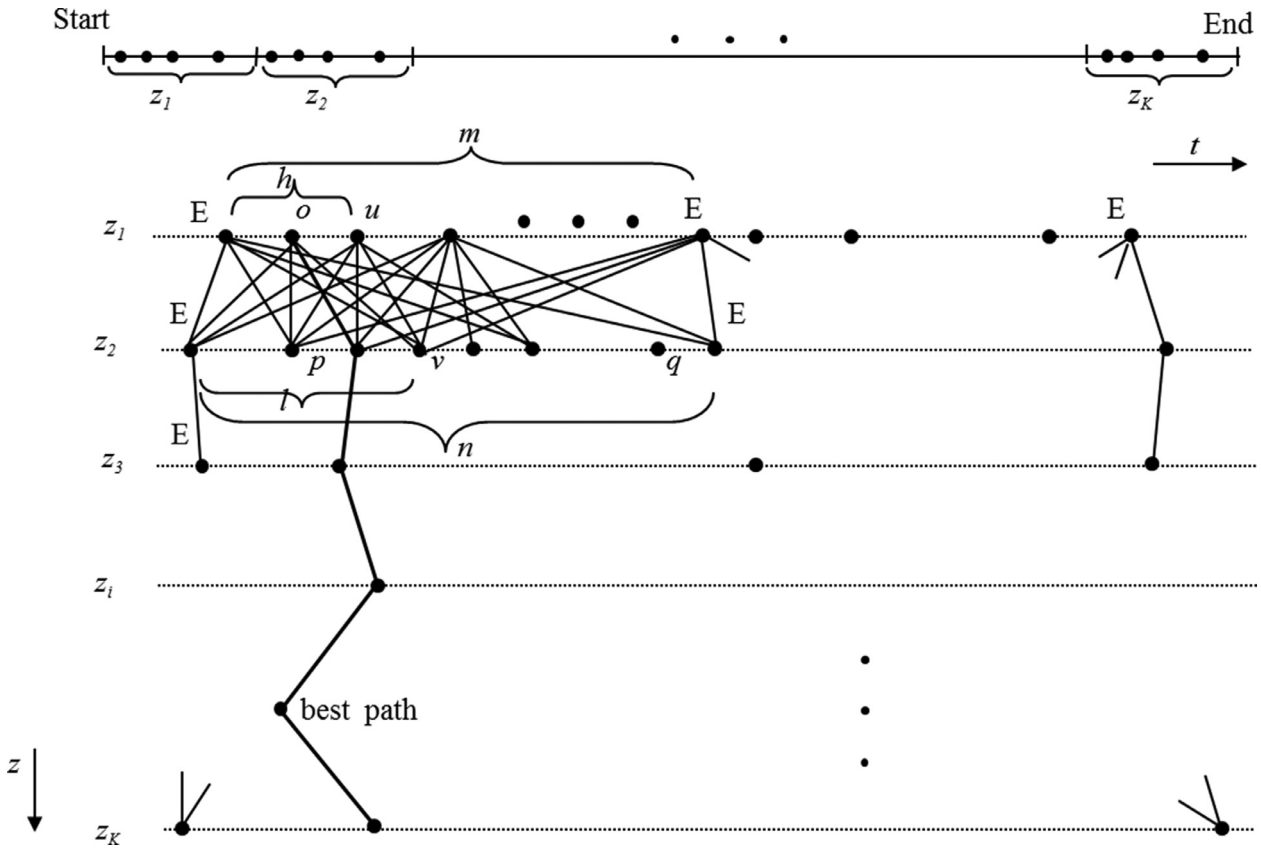


Fig. 1. A graphical representation of the 4D construction methodology. The top part indicates the entire time line from Start to End of patient scan with the time slices for each z -slice location marked on this line by heavy dots. The bottom part illustrates the graph built for finding the best 4D image. All nodes (time slices denoted by heavy dots) for a given z slice z_i are connected to all nodes for z_{i+1} . The E nodes denote time slices corresponding to end expiration. Please see text for the meaning of other variables.

2.3. 4D image construction algorithm

2.3.1. Stage1: Determining breathing phases $\varphi(t)$ and labeling reference nodes

At each z -location along the corresponding horizontal line, z_i , in Fig. 1, we mark each breathing period by examining all time slices and labeling slices corresponding to end expiration as E nodes. In fact, slices corresponding to end inspiration can also be used. The key here is not as to which reference nodes are to be used but to set up breathing cycles by labeling reference nodes. We find that E nodes are easier to locate than nodes corresponding to end inspiration, hence we use them in this work. At present this marking is done manually by observing the motion of the diaphragm. In the future, this step will be automated. All slices (bold dots or nodes on the horizontal line) lying between a slice labeled E and the next slice labeled E along that line constitute one breathing period. If the slices $f_n, f_{n+1}, \dots, f_{n+m}$ represent k th such period, then we consider these slices as being spread over m equally distributed phases of the breathing cycle for this particular E to E interval. That is, we let $T_k = \{\tau_0, \dots, \tau_m\}$ be the set of equally distributed m points on the circle C , with $\tau_j = \langle \cos(\frac{2\pi j}{m}), \sin(\frac{2\pi j}{m}) \rangle$, and define $\varphi(t_{m+j}) \approx \tau_j$ for $j \in \{0, \dots, m\}$. Finally, we define T as T_k of the smallest size. Note that the precision with which this identification is made is not that critical, since best 3D scenes are found by path optimization as we explain below. This assumption of equispacing on C is inevitable since we do not have any other information such as the time stamp with respect to the specific cycle as to when a slice within that cycle was acquired. If such information becomes available in the future then the assumption can be easily removed from our methodology. Note also that we do

not require any form of “resampling” of any cycle for changing the number of time points in the cycle since cost is estimated based on “distance” between time points by using the phase circle C under the assumption of uniform spacing of time points in each cycle although the number of points on the circle due to two different cycles may be different; see description under Stage 2. The reason for finding the smallest cycle T_k is to build the optimal 3D scenes starting from each time point in T_k . We wish to point out that every constructed optimal 3D scene and hence the final optimal 4D scene that is output will consist of only the original acquired slices and there is no interpolation of any form performed in the entire construction process.

2.3.2. Stage 2: Determining optimal 3D images via optimal path searching in a graph

Building a weighted graph: A graph $G=(A, P, w)$ is constructed to represent the relationship among the slice images f_i in terms of their potential spatial contiguity, as illustrated in Fig. 1. The slices in A form the nodes of the graph and each arc in the set P of arcs (solid lines in Fig. 1) represents a pair of slices $\{u, v\}$, where u and v are any slices from two adjacent z -locations. Note that the dotted horizontal lines in the figure are only for indicating the z -locations of the slices and do not represent arcs.

Each arc $e = \{u, v\}$ is given a weight or cost $w(e)$, also written as $w(u, v)$, to express the degree of unlikeliness of the slices u and v to come from the same time-frozen anatomic volume. $w(u, v) \in [0,1]$ and the smaller weight value close to zero means u and v are similar to each other and they are very likely to have come from the same phase. We compose $w(u, v)$ with the following three components: $w_g(u, v)$ that depends on the difference in gray inten-

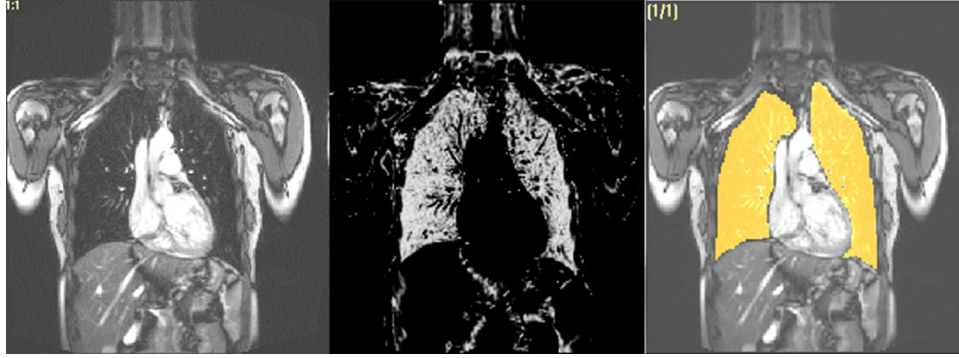


Fig. 2. Left: Original slice from a dynamic scan. Middle: Enhanced image. Right: lung segmentation.

sity of the slices u and v ; $w_s(u, v)$ that depends on the sign which expresses the directionality of motion (see below); and $w_p(u, v)$ that depends on the difference in z -positions of u and v . These components are combined via the formula $w(u, v) = w_g(u, v) \cdot w_s(u, v) \cdot w_p(u, v)$, and their individual formulations are described below.

Rather than using a straightforward root mean squared difference between the pixel intensities of slices u and v for determining the value of $w_g(u, v)$, we exploit knowledge of the appearance of the slice images and of the specific objects that move most conspicuously in $B(t)$. For example, in the thorax, the base of the lungs moves the most, and, since the lungs typically appear dark in MR images, we weight the changes from u to v from dark to brighter intensities more heavily than other changes. This is implemented by enhancing lungs via an image transformation which includes intensity thresholding operation within the body region for rough segmentation of the lungs and a morphological opening operation (erosion + dilation) for removing noise and non-lung tissues, as shown in Fig. 2.

More refined lung segmentation methods (Udupa et al., 2014) may be utilized but we feel that this is not needed. The image on the right in Fig. 2 is a segmentation of the lungs overlaid on the MRI slice. Compared to the enhanced image, no significant difference in the moving (lung) region of focus, since the other parts of body are almost static. The weight $w_g(u, v)$ is then defined by using the intensity distance between the enhanced slice images I'_u and I'_v at nodes u and v as follows,

$$w_g(u, v) = 1 - \exp\left(-\sum_c (I'_v(c) - I'_u(c))^2\right), \quad (1)$$

where c represents pixels in the images I'_u and I'_v .

The second component $w_s(u, v)$ takes into account slice-to-slice contiguity in both the direction of motion and spatial shape change in the t and z dimensions. This is one of the key ideas in our approach which brings power to the method in ensuring that the slices are ordered correctly within the approximation that is feasible given the way slices are acquired in free breathing. Considering the time component first, at slice position z_2 , see Fig. 1, suppose slices p and q are close in appearance to slice o at z_1 and they have the same intensity difference from o . Here we will prefer slice p to be considered to be closer to slice o since both p and o are in the inhalation phase in one respiratory period. That means two nodes from the same part of the respiratory period like o and p should be considered closer to each other than when they come from different parts, even when the intensity distance is the same, such as o from the inspiratory part and q from the expiratory part. In the phases corresponding to inhalation, less diaphragm excursion is visible, and for exhalation, more diaphragm excursion takes place. We use the sign of the difference of the average pixel in-

tensity values to show the breathing directional orientation. The idea for continuity in the z -direction is a bit more complex. Basically, we would insist that, the enhanced portions of the image (in our case, lungs) in slices u and v in two successive z locations should change spatially, in the sense of sign, in the same way the enhanced portions change in the slices corresponding to the respective E nodes on the *left* of slices u and v (“left” is arbitrary, we may instead choose “right” as well). That is, to be included in the same spatial volume corresponding to a fixed phase, the z -slices need to follow the sign pattern observed in their reference E nodes. Let $I'_{E,u}(c)$ and $I'_{E,v}(c)$ be the enhanced image intensities at pixel c for the reference nodes of slices of u and v , respectively. Combining the above ideas, $w_s(u, v)$ is given by

$$w_s(u, v) = \begin{cases} 2 \times S\left(\left|\sum_c (I'_v(c) - I'_u(c))\right|\right) - 1, & \text{when } \left[\sum_c (I'_v(c) - I'_u(c))\right] \times \text{sgn}_{u,v} \geq 0, \\ 1, & \text{otherwise.} \end{cases} \quad (2)$$

In this expression, $S(x) = (1 + \exp(-x))^{-1}$ and $\text{sgn}_{u,v} = \text{sign}(\sum_c (I'_{E,v}(c) - I'_{E,u}(c)))$, where the function $\text{sign}(y)$ takes on values 1, 0, and -1, respectively, when y takes on positive, zero, and negative values. In words, the top line of Eq. (2) corresponds to the situation when slices u and v follow the same sign as that of their reference E nodes for the change, and the bottom line refers to the case when the signs are opposite. In the latter case, $w_s(u, v)$ takes on the highest possible value 1. In the former case, the value is set inversely related to the magnitude of the total difference over all pixels between $I'_u(c)$ and $I'_v(c)$. It turns out that when time and spatial contiguity are addressed through w_s in this manner, 3D spatial volumes in each constructed 4D image change smoothly as well from one time instance to the next.

The idea behind the third component $w_p(u, v)$ is to assign a higher weight whenever the distance between their phase locations $\varphi(t_i)$ and $\varphi(t_j)$ is greater, where t_i and t_j denote respectively the time instances corresponding to u and v in $[0, \tau]$. That is, if u and v are similarly positioned within their respiratory periods, then they will be considered *close* and the weight will be low. The weight will increase with the degree of mismatch in their respiratory phases. The weight is given by

$$w_p(u, v) = (1 - e^{-d}) / (1 - e^{-1}), \quad (3)$$

where $d = \left| \frac{\min(h, m-h)}{m} - \frac{\min(l, n-l)}{n} \right|$, m and n are the numbers of slices (time points) in the periods where respectively u and v are located, and h and l denote respectively the offsets of u and v from their reference E nodes, as illustrated in Fig. 1. Smaller weight val-

Table 1
Image data sets used in evaluation.

Subject	Age	Voxel size (mm ³)	Slice size, number of time instances	Number of z-locations	Imaging plane (number of scans)	Imaging parameters	Number of breathing cycles
Adult-1	30	2.21 × 2.21 × 4.8	192 × 192, 35	31	Coronal (1)	T2-weighted; TR/TE = 60.06/1.15 ms	3
Adult-2	23	2.08 × 2.08 × 3.6	162 × 192, 100	50	Coronal (1)	T2-weighted; TR/TE = 214/1.55 ms	10
Child-1	10	1.17 × 1.17 × 5.0	224 × 256, 80	34	Sagittal (1)	T2-weighted; TR/TE = 4.48/2.24 ms	9
Child-2	9/11	1.09 × 1.09 × 5.0 1.17 × 1.17 × 5.0	224 × 256, 80	38/43	Sagittal (2)	T2-weighted; TR/TE = 3.88/1.94 ms	10
Child-3	6	1.07 × 1.07 × 5.0	224 × 256, 80	29	Sagittal (1)	T2-weighted; TR/TE = 3.90/1.95 ms	12
Child-4	7	1.09 × 1.09 × 5.0	224 × 256, 80	32	Sagittal (1)	T2-weighted; TR/TE = 4.48/2.24 ms	11
Child-5	5/6/8	1.17 × 1.17 × 5.0	224 × 256, 80	35	Sagittal (3)	T2-weighted; TR/TE = 3.88/1.94 ms	16
Adult-1	30	0.73 × 0.73 × 2.25	192 × 192	31	Coronal (2)	Breath-hold at end inspiration and end expiration; T2 weighted; TR/TE = 4.33/1.97 ms	–
Phantom	–	1.17 × 1.17 × 3.0	224 × 256, 80	60	Sagittal (1)	T2-weighted; TR/TE = 4.48/2.24 ms	12
Phantom	–	0.94 × 0.94 × 3.0	320 × 320	80	Sagittal (2)	T2-weighted; TR/TE = 900/84 ms	–

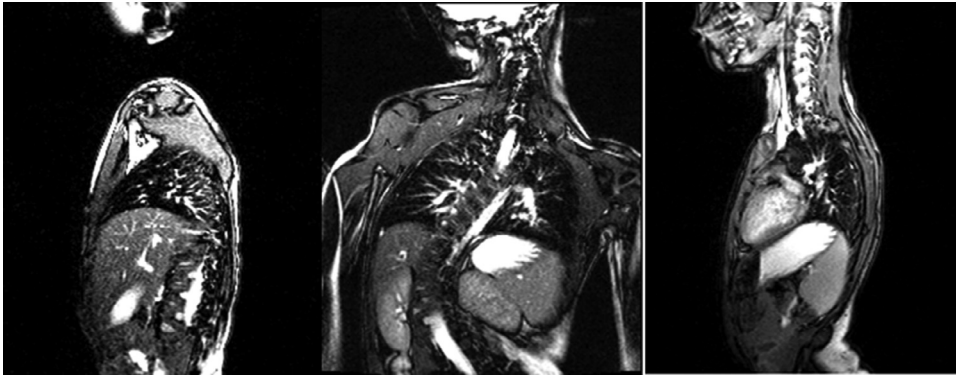


Fig. 3. Three sample slices – sagittal, coronal, and sagittal - from a pre-operative data set of Child-1.

ues (larger than zero) mean higher likelihood for u and v to have similar phase.

Combining the three components, the final weight $w(u, v)$ for arc $\{u, v\}$ is defined by

$$w(u, v) = w_g(u, v) \cdot w_s(u, v) \cdot w_p(u, v). \quad (4)$$

3D image construction via optimal path search: Once graph G is built, an optimal 3D image is constructed for each of a selected set of respiratory phases by using Dijkstra's algorithm and searching for an optimal path for each $\mu = f_i$ for which the corresponding breathing period T_k is of the smallest size, that is, $T_k = T$. For each such $\mu = f_i$, we find a path $A_\mu = \langle f_{n_1}, \dots, f_{n_k} \rangle$ in G such that: each f_{n_j} represents a slice with its z-coordinate being z_j ; the path contains f_i , that is, $f_i = f_{n_m}$ for some m ; both paths $\langle f_{n_1}, \dots, f_{n_m} \rangle$ and $\langle f_{n_m}, \dots, f_{n_k} \rangle$ are optimal. We consider each such constructed path A_μ as a 3D image for the respiratory phase $\varphi(t_i) \in T$.

2.3.3. Stage 3 - Constructing an optimal 4D image

Consider all sequences $S_k = \langle f_n, f_{n+1}, \dots, f_{n+m} \rangle$ of slices with the associated breathing period T_k equal to T . With each f_i from such S_k , we have associated a 3D image $F_i = A_{f_i}$ found in Stage 2. Then $B^k = \langle F_n, F_{n+1}, \dots, F_{n+m} \rangle$ is a 4D image representing one full breathing cycle. We choose one of these 4D images B^k , having the smallest cost, as the final output of our process. The cost of $B^k = \langle F_n, F_{n+1}, \dots, F_{n+m} \rangle$ is defined as the mean of the costs of the 3D images $F_n, F_{n+1}, \dots, F_{n+m}$, as used in Stage 2.

3. Experiments, evaluation, and discussion

3.1. Image data

3.1.1. Human subjects

Image data sets utilized in our evaluation all pertain to thoracic MRI and are summarized in Table 1. This retrospective study was conducted following approval from the Institutional Review Board at the Children's Hospital of Philadelphia along with a Health Insurance Portability and Accountability Act waiver. The data sets consist of 10 dynamic MRI scans from 7 subjects, including 2 adults and 5 children. Multiple MRI scans for the same subject correspond to different patient conditions like pre- and post-surgery as well as different imaging planes such as sagittal and coronal orientations. In our set up, for each (coronal or sagittal) slice position, slice images are acquired at a rate of about 200 ms/slice over several natural breathing cycles. For any subject, the total number of slices involved in 4D image reconstruction equals the product of the number of time instances and z locations acquired. This number for our subjects varies from 31×35 (~ 1000) (Adult-1) to 50×100 ($= 5000$) (Adult-2, see table), which contain both the anatomic and dynamic information about the thorax. The number of imaged cycles over all subjects varies from 2 to 16. The number of cycles for static images is shown as -.

Child-5 had two pre-operative scans and one post-operative scan. Adult-1 subject also had breath-hold images at end inspiration and end expiration. Sample slices from one of the pre-operative data sets of Child-1 are shown in Fig. 3, where we may



Fig. 4. A lung phantom constructed by 3D printing based on the real lung shape derived from a static MRI image of a petite adult subject. Realistic tidal breathing effect by air volume and respiratory rate is simulated by pumping air into and out of the lung shell. See text for details.

notice the significant malformations of the chest wall, lungs, and spine.

3.1.2. Dynamic MRI phantom

To more closely understand the behavior of the algorithm, we conducted the following phantom experiment.

In real patient data, it is difficult to establish truth, especially in this application of motion understanding. Unfortunately, in phantom experiments, authenticity of reality becomes questionable. Although this dichotomy is difficult to overcome, phantom experiments are helpful to understand the behavior of the algorithm.

An MRI-compatible dynamic lung volume phantom was designed as shown in Fig. 4. The phantom provides for dynamically varying a lung-shaped air volume by displacement of water, while being MR imaged. Imaged air volumes can be set to be either static, or time varying, depending on how air is pumped in and out of the phantom.

Construction: A hollow 3D-printed (Stratasys, Eden Prairie, MN) rigid polymer shell was made based on a segmented MRI image of a small adult's lungs, bronchi, and trachea at rest volume. The interior wall of the 3 mm thick shell preserves the complex external shape of the natural lungs. Total internal volume of the two lung shells is 1970 cc. The lungs-shell was opened at the apex of each lung and attached to a PVC pipe air delivery manifold that anchors it in an enclosing 0.25" thick Plexiglas tank. The base of each lung was provided with vent holes to allow water to fill and empty from

the shell into the tank as it is displaced by air. A hose to deliver the air volumes leads to either a manually driven calibrated volumetric syringe (Hans Rudolph, Shawnee, KS), or a programmable computerized piston (ASL 5000 Breathing Simulator, Ing Mar Medical, Pittsburgh, PA). The entire apparatus including the tank has dimensions of 28 cm H x 28 cm W x 19 cm L, and rests on the scanner bed inside the magnet bore.

Operation (as a simulation of tidal breathing): Initially, the tank is filled with water to the lung apex, which completely fills the lungs-shell with water. The hose is attached and a fixed static volume of air is delivered to the lungs with a calibrated syringe, displacing water downward. This volume is chosen to simulate a resting Functional Residual Capacity (FRC), in a natural lung shape. Then, an additional volume of air is delivered and withdrawn in an oscillating fashion using a second calibrated syringe, to simulate a tidal volume (TV) at a known breathing rate (BR). Although the shell is rigid, the air volume size and peripheral shape at the base change as the water interface rises and falls, approximating to some degree the shape change of the lungs during diaphragmatic motion. A dynamic MRI scan was performed at the following setting: BR = 20 cycles/min, FRC = 600 ml, TV = 200 ml. "Breath-hold" images were also acquired by stopping the second syringe exactly at end expiration, end inspiration, and mid respiratory phase. Image acquisition parameters were similar to those used for scanning human subjects, as listed in Table 1. Fig. 5 shows a sequence of time slices over one "respiratory" cycle for a fixed z location. An animation depicting this dynamic periodic movement is accessible via the link www.mipg.upenn.edu/Vnews/Lung_Phantom/Phantom_loc15.avi.

3.2. Evaluation of 4D constructed images

3.2.1. Qualitative

All constructed 4D images were visualized (Grevera et al., 2007) in both space and time in a cine slice mode by holding one variable fixed and letting the other change. This allowed close scrutiny of the overall accuracy of 4D construction in terms of the spatial and temporal contiguity of the slices of the 4D scene. An entire 4D volume can be examined visually quickly in this manner and discontinuities if any can be caught. A similar assessment was also made via 3D surface renditions. Contiguity in the z-dimension will manifest itself as smoothness of the 3D surface of the pleural space corresponding to each fixed time point of the 4D scene. Animation of this 3D rendition in time would qualitatively portray time contiguity of the dynamic 3D structure. All 4D constructions were found to be spatially and temporally contiguous when visualized in this manner in cine mode in both slice and 3D forms of visualization.

In the literature, *Random Stacking* is used as a reference method with which new 4D image construction strategies are compared (Siebenthal et al., 2005, 2007). We employed this method as well and implemented it as follows. First, for each time point t at the z_1

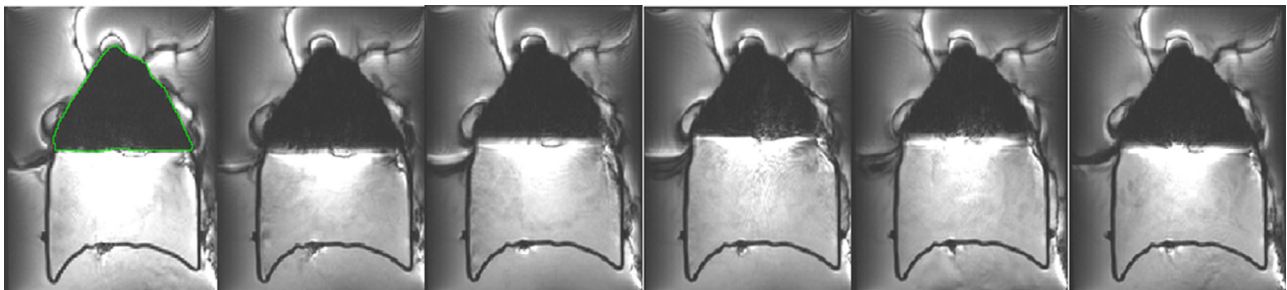


Fig. 5. Lung phantom time slices over one cycle at the same z location with the dark region representing the air volume. The dynamic change of the water-air interface simulates diaphragmatic motion.



Fig. 6. All z -slices from the constructed 4D image at one fixed time point for Adult-1 data set. Top 4 rows: From the proposed method. Bottom 4 rows: From random stacking. Red arrows in the 5th, 6th, and 7th rows point to the dome of the diaphragm for showing the difference between the two approaches: The motion from random construction is not as consistent as that from the proposed approach.

slice location, one slice at each location z_2, \dots, z_K is selected randomly from among all its time slices. These slices are put together to form one 3D spatial volume corresponding to time point t . Next, from all 3D spatial volumes so generated, x volumes are randomly selected where x denotes the number of time points in the optimal 4D volume constructed by our method. Note that there is some order in the random selection, in the sense that, for a fixed t position, randomness is only in the time dimension for each z -po-

sition; similarly once spatial volumes are constructed, randomness is in the t dimension only. Clearly the constructed 4D scene is not a collection of the requisite number of slices selected totally randomly from all acquired slices. We use Adult-1 data set to compare visually our optimal construction method with Random Stacking. In this example, the constructed optimal 4D scene had spatial dimensions of $192 \times 192 \times 31$ and the number of time points in the optimal period was 10. The 4D construction process thus selected

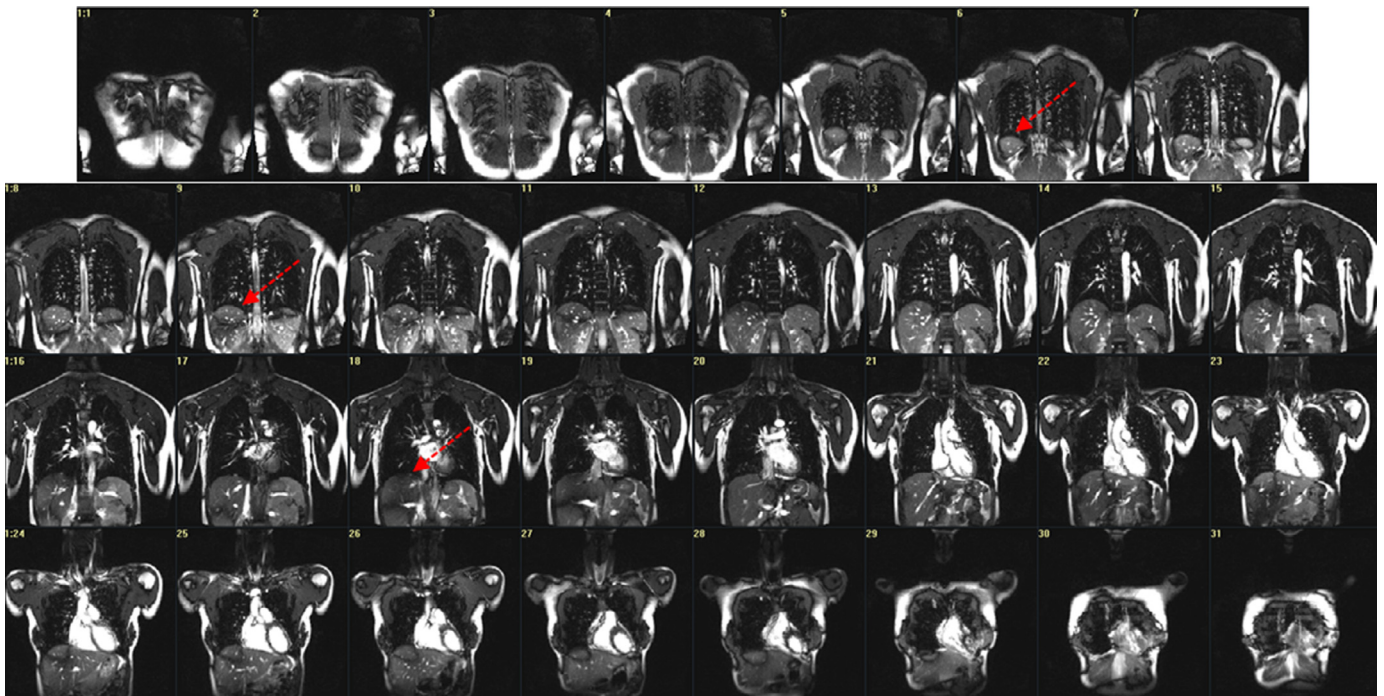


Fig. 7. All z-slices from a 3D image corresponding to a time position in a 4D image constructed by employing only intensity weight. Compared with the image constructed by utilizing all three weights, the intensity-only approach fails as shown by the red arrows where the dome of the diaphragm appears to indicate change of surface contour that is counter to a smooth surface.

an optimal set of 310 slices over one breathing period from the acquired set of $31 \times 35 = 1085$ slices.

In Fig. 6, all z-slices corresponding to a fixed respiratory phase for the two methods are displayed. The constructed 3D volume image at each time point should be consistent, meaning in particular that the diaphragm surface should change smoothly spatially. Although intensity is the main factor for defining the similarity of neighboring slices, the intensity-only approach for searching the optimal path often fails, as illustrated in Fig. 7. When only intensity weighting is employed for searching the most similar slices between neighboring slice locations, the resulting optimal 3D volume is worse than that using all three weight factors (Fig. 6). The images with red arrow in Fig. 7 show the wrong slices that were selected to construct the optimal 3D volume image where the diaphragm surface is spatially not as smooth as in the image constructed by utilizing all three weight factors.

Fig. 8 shows all time-slices for a fixed z-position. Better spatial contiguity and consistency of the slices in Fig. 6 is evident for the optimal method over Random Stacking (see the superior aspect of the liver marked by red arrows). Similarly in Fig. 8, optimally constructed slices are more consistent temporally than slices from Random Stacking; observe the change in the position of the diaphragm which appears periodic in the former but somewhat chaotic in the latter method as shown in the slices marked with red arrows. This difference in behavior is better appreciated in a cine mode of display where we have verified for all z and t positions the same observation.

In Fig. 9, we demonstrate the similarity for images at end inspiration and end expiration between the optimally constructed image and the acquired breath-hold image for Adult-1. Although the image quality of the breath-hold scan is better than that of the dynamic scan (see Table 1), we note that the end inspiration and expiration images and the diaphragm and chest wall excursions are very similar for the two modes. The figure shows segmented pleural space overlaid on the images as well as the differ-

ence between the segmented pleural spaces from end inspiration to expiration. Finally, surface renditions of the 10 3D pleural spaces corresponding to the 10 time instances from the optimally constructed 4D scene are shown in Fig. 10. All surface renditions are set up from the same viewpoints. Not only the surface renditions but also the location change / motion among 3D pleural spaces can be found. The smooth motion of the surface can be appreciated from the rendered images, especially when the renditions are animated.

3.2.2. Quantitative

Based on patient data: There are two important features of the dynamic thorax which we will exploit for the purpose of our quantitative evaluation – smooth variation of the area of the pleural space from slice to slice over a spatial volume corresponding to a fixed respiratory phase and the (quasi) periodic motion of the diaphragm. A third form of evaluation we will demonstrate is a comparison of the lung volume obtained for the adult subjects from their breath-hold static image to a spatial volume obtained from their optimally constructed 4D image corresponding to roughly the same respiratory phase. Unfortunately, this experiment cannot be conducted on our pediatric patients since they are under anesthesia and unable to hold their breath to facilitate acquiring static images. These evaluations are described below.

Let B^k denote the optimally constructed 4D image. We will denote the area of the pleural space in a slice corresponding to time t and spatial location z in B^k by $\alpha(t, z)$. We will characterize the smoothness of the variation of this area curve with respect to z for three fixed time points $t_1 = \text{end expiration}$, $t_3 = \text{end inspiration}$, and $t_2 = \text{mid-respiratory phase}$. That is, we will evaluate the derivative of the area curves $\alpha(t_1, z)$, $\alpha(t_2, z)$, and $\alpha(t_3, z)$ obtained for B^k and compare them with derivatives of similar curves $\alpha_r(t, z)$ obtained for the image resulting from random stacking. Fig. 11 displays the derivative curves of the right lung for the two methods obtained for the dynamic data sets in Table 1. For the top three

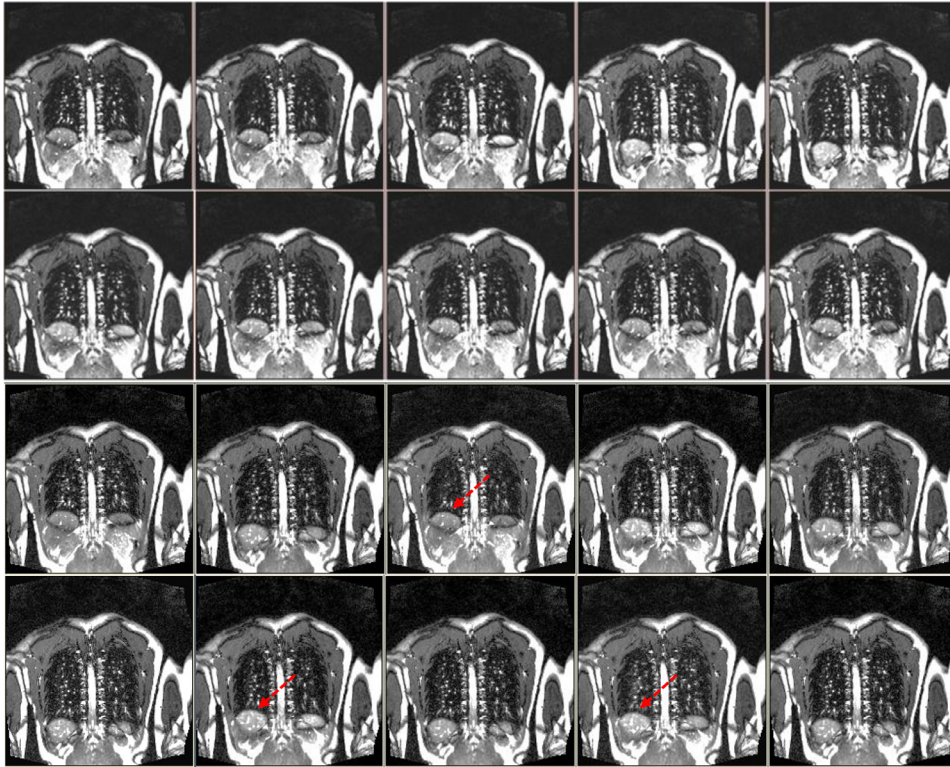


Fig. 8. All t -slices from the constructed 4D image over one period (10 time points) for one fixed z -position for Adult-1 data set. Top two rows: From the proposed method. Bottom two rows: From random stacking.

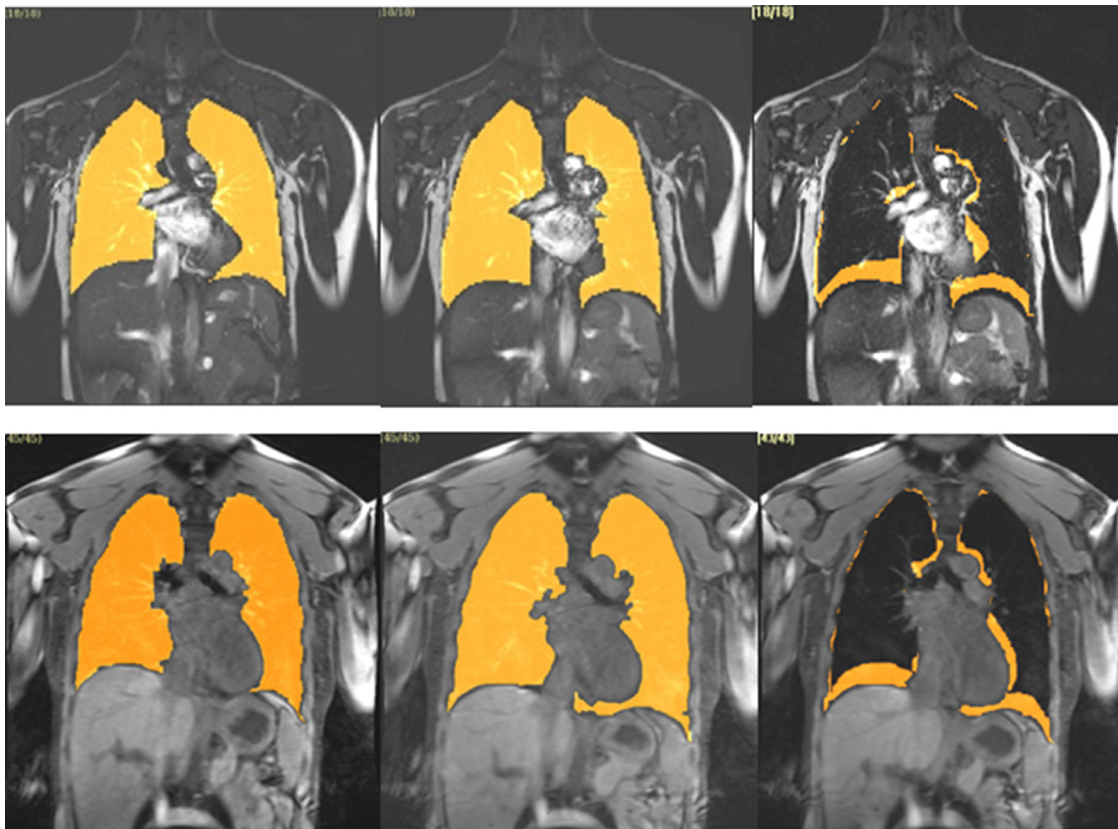


Fig. 9. Top: Slices from end-expiration and end-inspiration with segmented pleural space overlaid for the 4D volume optimally constructed from Adult-1 data set. The third column shows the difference of segmentations overlaid on end inspiration image. Bottom: Same arrangement as top row except the images are from the breath-hold scan for Adult-1.

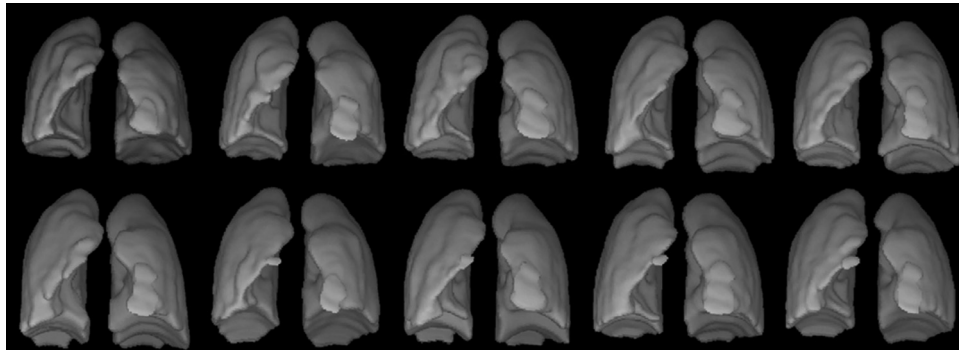


Fig. 10. Surface renditions of the 10 volumes over one respiratory period (top left to bottom right) created from the optimally constructed 4D volume of Adult-1 data set.

Table 2

Lung volume comparison (in cc) between breath-hold and 4D constructed scenes.

Subject	End-inspiration		End-expiration		Change (%)
	Breath-hold	4D	Breath-hold	4D	
Adult-1	2675.03	2523.75	2207.68	2217.95	3.1
Phantom	800.00	735.94	600.00	614.2	3.5

Table 3

Running time (in seconds) for different stages of the 4D construction method.

Stage 1	Stage 2	Stage 3
10–20 sec/z-location	64.30	0.09

rows in Fig. 11, the different colors represent the result for different subjects. The results are similar for the two lungs and hence shown only for one lung. We note that the derivative curves are much smoother for the optimal method than for random stacking at all three time points. Further, the behavior is similar for all subjects for the optimal method but not so for random stacking. The pattern of change of area in the z -direction may be expected to be similar for all subjects. To illustrate this point, in the last row of Fig. 11, we display the area curves for both methods for Adult-1 for t_1 and t_3 together with the area curves obtained for Adult-1 from the static images acquired at similar breath-hold positions. Clearly the optimal method follows the curve pattern of the static images correctly while random stacking does not. In these plots, the horizontal axis indicates slice number and the vertical axis denotes the area derivative in mm^2/mm (top three rows) and area in mm^2 (last row).

To illustrate the time contiguity achieved by our algorithm, in Fig. 12, we display the height $\eta(t, z)$ (in mm) of the apex of the left and right hemi diaphragms from the bottom edge of the slice as measured on the slice corresponding to t for a fixed z for both methods. For each subject and each method two curves are obtained – corresponding to the left and the right hemi diaphragms. The z -slices are taken roughly passing through the apex of the diaphragm domes. The idea is that this location is the most sensitive for observing how well periodicity of the respiratory motion is captured by the methods. As seen in the figure, for both z -slices, the optimal method achieves consistent time ordering of the slices whereas random stacking leads to a chaotic behavior, especially on adult data. Also interestingly, the location change for adults during one period is more significant than children with TIS. That is reasonable since for normal adults the excursion of the diaphragm can be expected to be more than for normal children, and especially those with TIS.

Table 2 shows a comparison of the lung volumes obtained from static images and optimally constructed dynamic images for roughly the same respiratory phase for the adult subject (Adult - 1). The static images can be considered as ground truth since they are of much better quality and they are obtained at one fixed lung volume, although the actual lung volume at which the subject held breath may not be exactly the same as the volume at the cor-

responding respiratory phase in his tidal breathing cycle. As seen from Table 2, the difference between the two volumes is about 3%.

Based on phantom data: Phantom analysis results similar to those in Figs. 9 and 10 are shown in Figs. 13 and 14. Height (in mm) curves are shown in Fig. 14 for a slice through the middle of the left and right lung. We note that for the same time point, height values are kept almost the same for the optimal method but not for random stacking.

Table 3 summarizes the running time in seconds for the different stages of the 4D construction process. Computational times for Stage 2 and Stage 3 are for MATLAB 2015a implementation on a Lenovo computer with the following specifications: 4-core, 3.7 GHz CPU (AMD A10-6700) with 16GB RAM, and running the professional Windows 7 operating system.

The proposed method is different from those reported in the literature in four respects. First, it is not based on finding a respiratory signal from the acquired data like most other approaches (Georg and Souvenir, 2008; Georg et al. 2008; and Wachinger et al., 2010, 2012), or acquiring explicitly respiratory signals (Cai et al., 2011) which would pose challenges in our application because of the practical difficulty arising from the very sick pediatric patients. Second, and as a consequence, it guarantees globally optimal solution as per the formulated combinatorial optimization criterion unlike other approaches. Third, most 4D construction methods reported in the literature are for CT images, the only exception we are aware of for MRI is the one from Wagshul (Wagshul et al., 2013). The issues encountered in MRI are quite different and more challenging since the image contrast, resolution and tissue properties portrayed are different in CT and MRI. Wagshul's approach is not based on image processing, instead it employs retrospective gating by utilizing tidal volume captured from airflow measurements to select useful respiratory data. Finally, we are not aware of any published methods that validated its approach based on a realistically constructed 4D phantom and the associated dynamic images.

Different criteria have been used for evaluating the 4D constructions. The cross-sectional area of the oropharynx of the reconstructed upper airway images has been used in Wagshul's paper (Wagshul et al., 2013) to evaluate the final constructed 4D image. Other criteria include comparison of the 4D image at a time point to breath-hold images (Siebenthal et al., 2005, 2007) acquired typically at end inspiration and/or end expiration. Breath-hold images

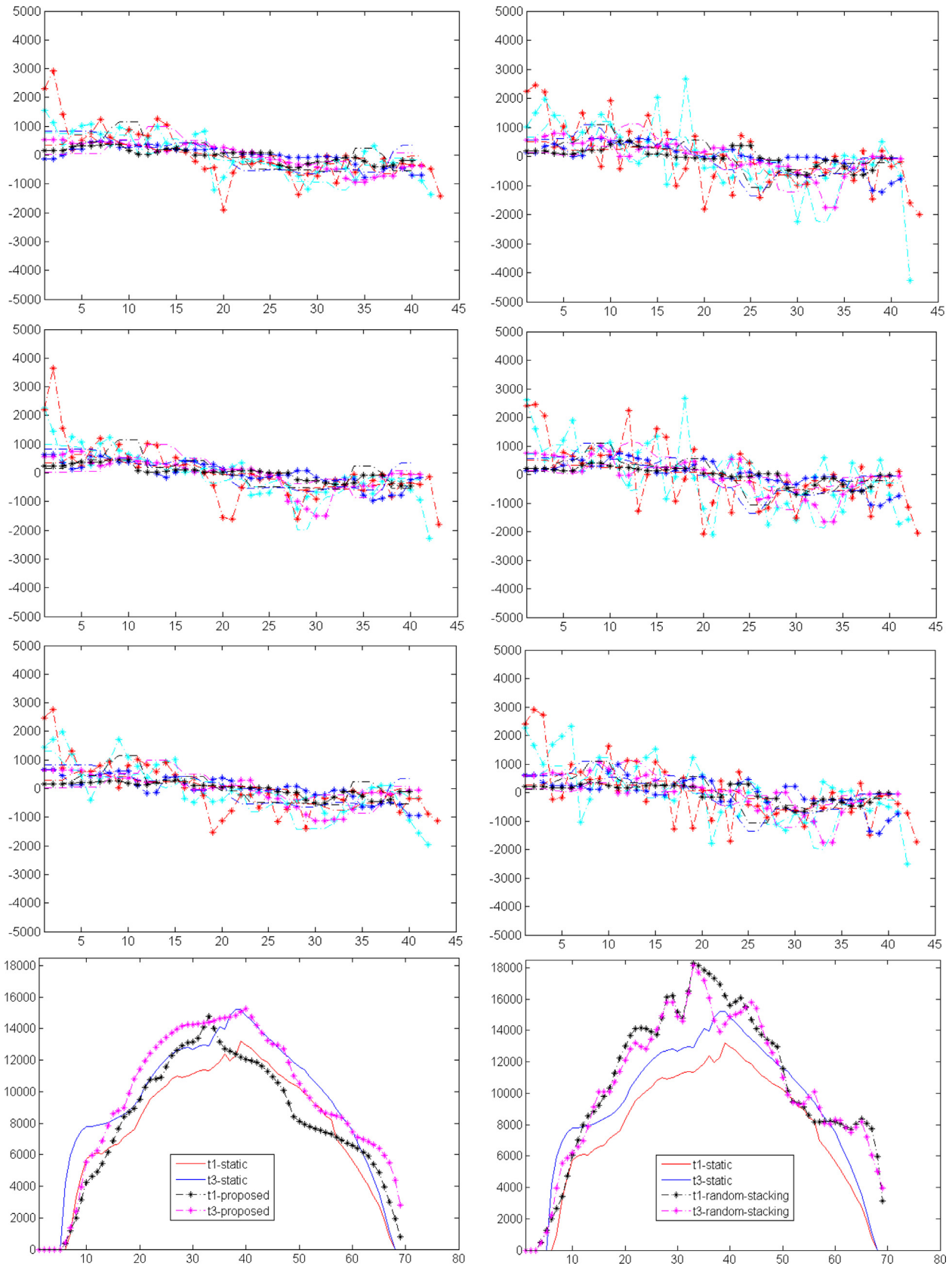


Fig. 11. Derivative of the area curves $\alpha(t, z)$ and $\alpha r(t, z)$ for the proposed method (left) and random stacking (right) for three time points $t1 = \text{end expiration}$ (1st row), $t3 = \text{end inspiration}$ (2nd row), and $t2 = \text{mid-respiratory phase}$ (3rd row) for the right lung. Curves for the left lung are similar. Different colors represent different subjects. In these curves, the vertical axis is in units of mm^2/mm and the horizontal axis shows z -slice number. The last row shows area curves (in mm^2) for Adult-1 for the two methods at $t1$ and $t3$ in comparison to similar curves obtained from breathhold images for this subject, the horizontal axis again showing the z -slice number.

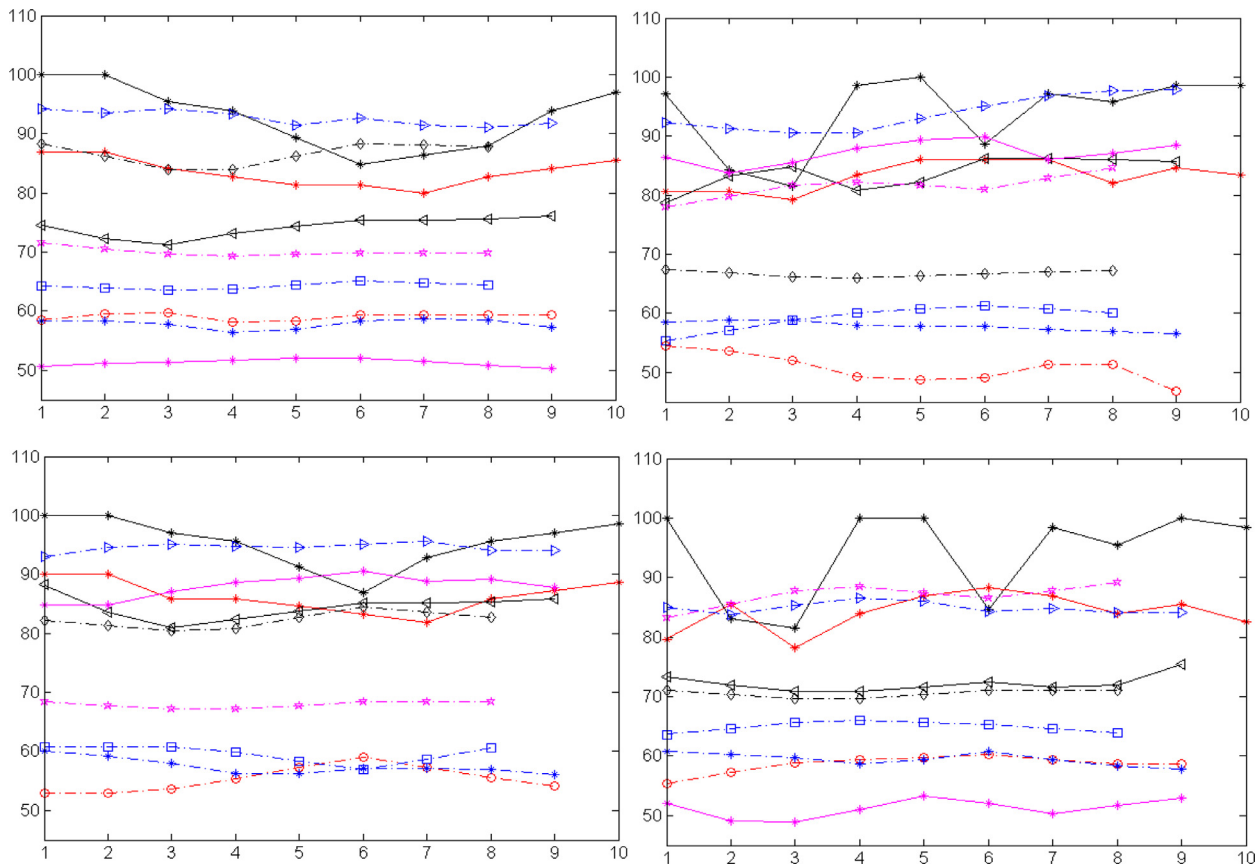


Fig. 12. Height curves $\eta(t, z)$ for the proposed method (left) and random stacking (right) for the 10 subjects. Two plots (top and bottom) are shown for each subject – corresponding to the height of the left and the right apex of the two hemi diaphragms. The height unit is in mm (vertical axis) and the horizontal axis denotes time. The different colors denote different subjects.

are difficult to acquire from our pediatric patients. This is why we have carried out this comparison on adult patients. Other volumes between those two special locations should be smoothly varying and consistent. Comparison to random stacking strategy is another approach commonly used (Siebenthal et al., 2005, 2007) which we have also adopted. For 4D construction methods which utilize free-breathing slice acquisitions, we feel that the phantom experiment we designed is ideal since it allows controlling breathing rate, tidal volume, and the shape of the pleural space.

4. Conclusions

In the study of many pediatric diseases that involve malformations of the thorax, dynamic MR imaging is essential in order to understand the specific biomechanical deficits of the respiratory engine. Because of the severity of the diseases and radiation concerns for CT, MR imaging under free tidal breathing without any encumbrance to the patient is the only modality that is appropriate for imaging these patients. We have presented a post hoc image construction method to select an optimal 4D image from the thousands of acquired slices. The method employs a unique combinatorial optimization approach and guarantees a globally optimal solution. We have presented its evaluation based on normal adult images as well as pediatric patient images. A 4D dynamic phantom created via 3D printing technology from image data from a normal subject has been designed and its dynamics have been used to further validate the method. The method is practical and can be used

routinely on dynamic MRI images of patients with thoracic insufficiency syndrome and other pediatric thoracic deformities where dynamic studies are called for.

One current shortcoming of the method is the human interaction required in Stage 1. This step takes roughly 5–10 min for coronal acquisitions (where the number of z-locations is about half as many as in sagittal) and 10–20 min for sagittal acquisitions. It is conceivable to automate this step following the same idea underlying graph-based optimization for breaking up each z-line into respiratory periods. It may be possible even to make this process also part of the entire optimization schema for possibly finding a globally optimal solution. Other possible future avenues include adaptation of the same method to dynamic CT and ultra sound images where only the parameters of the cost function will need to be modified. Validation of these methods on real patient images is a challenge since establishment of hard truth becomes really difficult. We will conduct evaluations on more patient and normal data sets along similar lines as described in this paper to gain more clinical confidence in the future. At present, in our TIS clinical conferences, each patient is discussed in a group setting consisting of clinicians and scientists, where the acquired slices (typically the mid coronal/sagittal) are visualized in a cine mode. In the future, we will use the 4D constructed images to produce spatio-temporal animations, which we believe may give us further insight into the 4D construction process and its characteristics. Another potential future avenue is building and validating on 4D phantoms printed from patient image data rather than normal subjects.

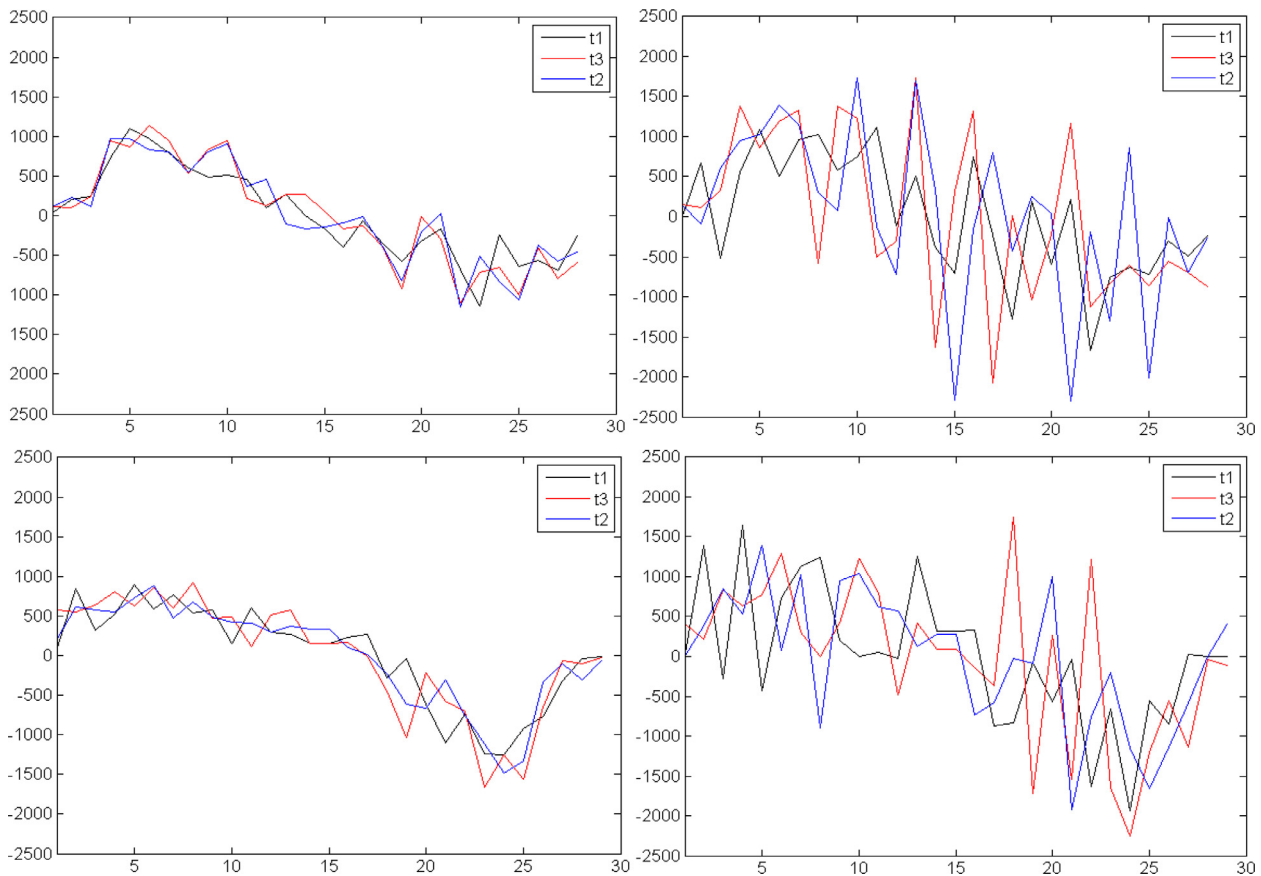


Fig. 13. Derivative of the area curves $\alpha(t, z)$ and $\alpha r(t, z)$ for the proposed method (left) and random stacking (right) for three time points t_1 = end expiration, t_3 = end inspiration, and t_2 = mid-respiratory phase for the phantom data. The vertical axis is in mm²/mm and the horizontal axis shows the z-slice number.

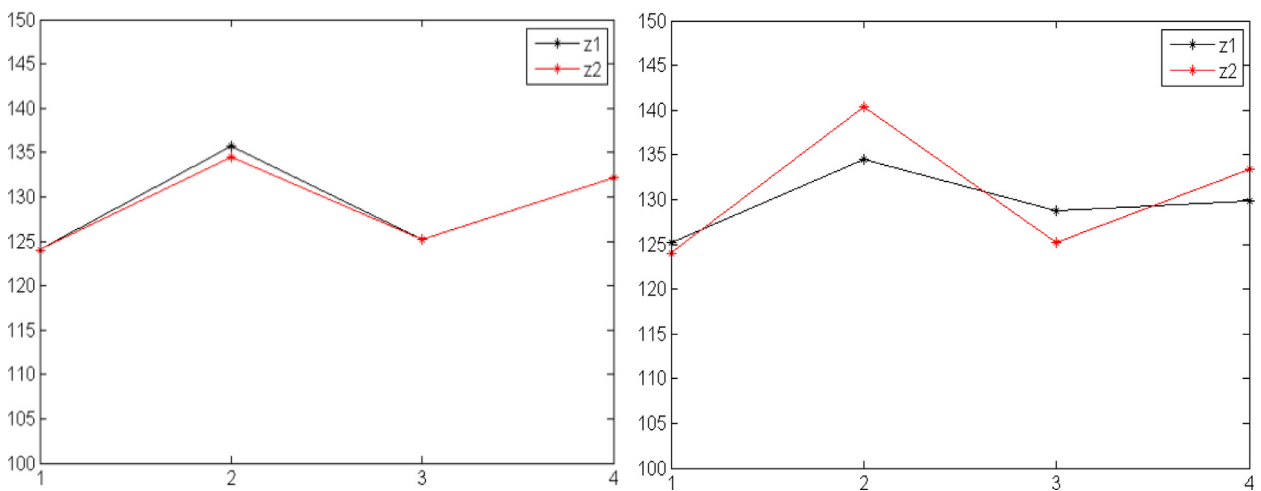


Fig. 14. Height curves $\eta(t, z)$ for the proposed method (left) and random stacking (right) for Phantom data. Two plots are shown – corresponding to the height of the left and the right apex of the two “hemi diaphragms”. The height unit is mm (vertical axis) and the horizontal axis denotes time points.

Acknowledgements

The research reported here is funded by a DHHS grant R21HL124462 and was partly supported in its initial stages by a grant from the Children’s Hospital of Philadelphia.

References

Cai, J., Chang, Z., Wang, Z., Paul Segars, W., Yin, F.F., 2011. Four-dimensional magnetic resonance imaging (4D-MRI) using image-based respiratory surrogate: a feasibility study. *Med. Phys.* 38, 6384–6394.

- Fayad, H.J., Lamare, F., 2013. Generation of 4-dimensional CT images based on 4-dimensional PET-derived motion fields. *J. Nucl. Med.* 54 (4), 631–638.
- Campbell Jr., R.M., Smith, M.D., Mayes, T.C., Mangos, J.A., Willey-Courand, D.B., Kose, N., Pinero, R.F., Alder, M.E., Duong, H.L., Surber, J.L., 2003. The characteristics of thoracic insufficiency syndrome associated with fused ribs and congenital scoliosis. *J. Bone Joint Surg.* 85, 399–408.
- Campbell Jr., R.M., Smith, M.D., 2007. Thoracic insufficiency syndrome and exotic scoliosis. *J. Bone Joint Surg.* 89A, 108–122.
- Georg, M., Souvenir, R., 2008. Manifold learning for 4D CT reconstruction of the Lung. *CVPRW2008* <http://doi.ieeecomputersociety.org/10.1109/CVPRW.2008.4563024>.
- Georg, M., Souvenir, R., Pless, R., 2008. Simultaneous data volume reconstruction and pose estimation from slice samples. *CVPR2008* <http://doi.ieeecomputersociety.org/10.1109/CVPR.2008.4587740>.

- Grevera, G., Udupa, J.K., Odhner, D., Zhuge, Y., Souza, A., Iwanaga, T., Mishra, S., 2007. CAVASS: a computer-assisted visualization and analysis software system. *J. Digital Imaging* 20 (Suppl 1), 101–118.
- Keall, P.J., Starkschall, G., Shukla, H., Forster, K.M., Ortiz, V., Stevens, C.W., Vedam, S.S., George, R., Guerrero, T., Mohan, R., 2004. Acquiring 4D thoracic CT scans using a multislice helical method. *Phys. Med. Biol.* 49, 2053–2067.
- Keall, P.J., Vedam, S.S., George, R., Williamson, J.F., 2007. Respiratory regularity gated 4D CT acquisition: concepts and proof of principle. *Australas. Phys. Eng. Sci. Med.* 30, 211–220 / supported by the Australasian College of Physical Scientists in Medicine and the Australasian Association of Physical Sciences in Medicine.
- Koste, S.J.R., Senan, S., Kleynen, C.E., Slotman, B.J., Lagerwaard, F.J., 2006. Renal mobility during uncoached quiet respiration: an analysis of 4DCT scans. *Int. J. Radiat. Oncol. Biol. Phys.* 64, 799–803.
- Li, G., Citrin, D., Camphausen, K., Mueller, B., Burman, C., Mychalczak, B., Miller, R.W., Song, Y., 2008. Advances in 4D medical imaging and 4D radiation therapy. *Technol. Cancer Res. Treat.* 7, 67–81.
- Li, R., Lewis, J.H., Cervino, L.I., Jiang, S.B., 2009. 4D CT sorting based on patient internal anatomy. *Phys. Med. Biol.* 54, 4821–4833.
- Liu, Y., Yin, F.F., Chang, Z., Czito, B.G., Palta, M., Bashir, M.R., Qin, Y., Cai, J., 2014. Investigation of sagittal image acquisition for 4D-MRI with body area as respiratory surrogate. *Med. Phys.* 41, 101902–101902.
- Low, D.A., Nystrom, M., Kalinin, E., Parikh, P., Dempsey, J.F., Bradley, J.D., Muttic, S., Wahab, S.H., Islam, T., Christensen, G., Politte, D.G., Whiting, B.R., 2003. A method for the reconstruction of four-dimensional synchronized CT scans acquired during free breathing. *Med. Phys.* 30, 1254–1263.
- Murphy, M.J., Balter, J., Balter, S., BenComo Jr., J.A., Das, I.J., Jiang, S.B., Ma, C.M., Olivera, G.H., Rodebaugh, R.F., Ruchala, K.J., Shirato, H., Yin, F.F., 2007. The management of imaging dose during image-guided radiotherapy: report of the AAPM Task Group 75. *Med. Phys.* 34, 4041–4063.
- Nandalike, K., Shifteh, K., Sin, S., Strauss, T., Stakofsky, A., Gonik, N., Bent, J., Parikh, S.R., Bassila, M., Nikova, M., Muzumdar, H., Arens, R., 2013. Adenotonsillectomy in obese children with obstructive sleep apnea syndrome: magnetic resonance imaging findings and considerations. *Sleep* 36 (6), 841–847.
- Nehmeh, S.A., Erdi, Y.E., Pan, T., Pevsner, A., Rosenzweig, K.E., Yorke, E., Mageras, G.S., Schoder, H., Vernon, P., Squire, O., Mostafavi, H., Larson, S.M., Humm, J.L., 2004. Four-dimensional (4D) PET/CT imaging of the thorax. *Med. Phys.* 31, 3179–3186.
- Nehmeh, S.A., Erdi, Y.E., Pan, T., Yorke, E., Mageras, G.S., Rosenzweig, K.E., Schoder, H., Mostafavi, H., Squire, O., Pevsner, A., Larson, S.M., Humm, J.L., 2004. Quantitation of respiratory motion during 4D-PET/CT acquisition. *Med. Phys.* 31, 1333–1338.
- Qi, H.P., Li, J.B., Zhang, Y., Wang, W., Li, F.X., Wang, S.Z., 2013. Comparison of the displacements of peripheral lung cancer based on 4D CT scan and 3D CT scan assisted with active breathing control. *Zhonghua zhong liu za zhi [Chinese journal of oncology]* 35, 514–517.
- Remmert, G., Biederer, J., Lohberger, F., Fabel, M., Hartmann, G.H., 2007. Four-dimensional magnetic resonance imaging for the determination of tumour movement and its evaluation using a dynamic porcine lung phantom. *Phys. Med. Biol.* 52, N401–N415.
- Siebenthal, M., Cattin, P., Gamper, U., Lomax, A., Szekely, G., 2005. 4D MR imaging using internal respiratory gating. *MICCAI* 8 (2), 336–343.
- Siebenthal, M., Cattin, P., Gamper, U., Boesiger, P., Lomax, A., Cattin, P., 2007. 4D MR imaging of respiratory organ motion and its variability. *Phys. Med. Biol.* 52, 1547–1564.
- Tong, Y.B., Udupa, J.K., Odhner, D., Ciesielski, K., 2014. Graph-based retrospective 4D image construction from free-breathing MRI slice acquisitions. *Proceeding of SPIE, Medical Imaging*, vol. 9038 9038011–9038017.
- Tory, M., Röber, N., Möller, T., Celler, A., Atkins, M.S., 2001. 4D Space-Time techniques: A medical imaging case study. In: *VIS01, Proc. IEEE Visualization*, pp. 473–477.
- Tsoumpas, C., Buerger, C., King, A.P., Mollet, P., Keereman, V., Vandenberghe, S., Schulz, V., Schleyer, P., Schaeffter, T., Marsden, P.K., 2011. Fast generation of 4D PET-MR data from real dynamic MR acquisitions. *Phys. Med. Biol.* 56, 6597–6613.
- Udupa, J.K., Odhner, D., Zhao, L., Tong, Y., Matsumoto, M.M., Ciesielski, K.C., Falcao, A.X., Vaideeswaran, P., Ciesielski, V., Saboury, B., Mohammadianrasanani, S., Sin, S., Arens, R., Torigian, D.A., 2014. Body-wide hierarchical fuzzy modeling, recognition, and delineation of anatomy in medical images. *Med. Image Anal.* 18, 752–771.
- Wachinger, C., Yigitsoy, M., Navab, N., 2010. Manifold learning for image-based breathing gating with application to 4D ultrasound. *MICCAI* 13, 26–33.
- Wachinger, C., Yigitsoy, M., Rijkhorst, E.J., Navab, N., 2012. Manifold learning for image-based breathing gating in ultrasound and MRI. *Med. Image Anal.* 16, 806–818.
- Wagshul, M.E., Sin, S., Lipton, M.L., Shifteh, K., Arens, R., 2013. Novel retrospective, respiratory-gating method enables 3D, high resolution, dynamic imaging of the upper airway during tidal breathing. *Magn. Reson. Med.* 70, 1580–1590.
- Wink, N., Panknin, C., Solberg, T.D., 2006. Phase versus amplitude sorting of 4D-CT data. *J. Appl. Clin. Med. Phys.* 7, 77–85 / American College of Medical Physics.
- Yang, D., Lu, W., Low, D.A., Deasy, J.O., Hope, A.J., 2008. 4D-CT motion estimation using deformable image registration and 5D respiratory motion modeling. *Med Phys.* 35 (10), 4577–4590.
- Zhang, J., Xu, G.X., Shi, C., Fuss, M., 2008. Development of a geometry-based respiratory motion-simulating patient model for radiation treatment dosimetry. *J. Appl. Clin. Med. Phys.* 9 (1), 2700 / American College of Medical Physics.